PERGAMON

International Journal of Heat and Mass Transfer 45 (2002) 3759–3770

International Journal of HEAT and MASS TRANSFER

www.elsevier.com/locate/ijhmt

Numerical simulations of a low power microchannel thermal cycling reactor

David Erickson, Dongqing Li *

Department of Mechanical and Industrial Engineering, University of Toronto, 5 King's College Road, Toronto, Ont., Canada M5S 3G8

Received 22 August 2001; received in revised form 16 February 2002

Abstract

A roadblock to the development of stand-alone microscale biomedical and chemical analysis systems is the relatively high heating power requirement of the microscale reactors, which typically exceeds the capability of low cost batteries. In this study, a microchannel thermal cycling reactor design using in-channel heating and passive cooling is proposed and a numerical model has been developed. Numerical simulations were conducted to determine the conditions under which efficient, rapid thermal cycling can be achieved with minimum heating power load. The simulations revealed that with a low thermal conductivity substrate and an optimized heater-channel configuration a microchannel reactor is capable of performing rapid thermal cycling to temperatures as high as 95 °C with as little as 20 mW/channel peak heating power.

1. Introduction

The proliferation of manufacturing techniques for building microfluidic components has led to a virtual explosion in the development of microscale chemical and biological analysis systems. Numerous studies have unveiled chip sized devices capable of conducting complex analytical procedures such as capillary electrophoresis [1], sperm testing and in vitro fertilization [2,3], and the polymerase chain reaction (PCR) [4,5] or ligase chain reaction (LCR) [6]. More recent works have led to the development of integrated devices that combine two or more procedures onto a single chip. For example Wilding et al. [7] presented a device that combines the PCR with cell isolation, Burns et al. [8] introduced a number of microfabricated structures for DNA analysis, and several others have worked to combine the PCR with capillary electrophoresis to form an integrated microscale DNA analysis system [9–12]. The ability of these devices to perform precise chemical analysis on extremely small samples brings significant advantages to biochemists and molecular biologist in terms of speed, cost and automation.

A crucial component of many of these lab-on-chip devices are the microscale reactors and thermal cyclers in which the desired chemical or biological reactions are to occur. The PCR, for example, is a common way to amplify small concentrations of DNA molecules by repeatedly processing the sample and some reagents through a thermal cycle as shown in Fig. 1, each time inducing a reaction that, ideally, increases the amount of DNA by a factor of 2. Though holding times and temperature levels can vary, a typical reaction is as follows. In Stage 1, the sample is heated to about 95 °C and held for approximately 5 s while the double stranded DNA is separated into two strands. In Stage 2, the sample is cooled to 60 °C and held for about 10 s while the Oligonucleotide primers that flank the DNA to be amplified are annealed. In Stage 3, the sample is heated to an intermediate temperature 75 °C and held for about 15 s while the target DNA are extended in the presence of a polymerization enzyme and deoxynucleotide triphosphates. This reaction allows a single DNA molecule to be copied as many as a billion times [5], making biochemical analysis of extremely small original samples possible. The ability to handle these extremely small samples and the potential for efficient thermal cycling,

* Corresponding author. Tel.: +1-416-978-1282; fax: +1-416-978-7753.

E-mail address: dli@mie.utoronto.ca (D. Li).

0017-9310/02/$ - see front matter
PII: S0017-9310(02)00091-1

Nomenclature

A_c	cross-sectional area of the channel (m^2)
Bi	Biot number, hD_h/k_s
D	non-dimensional electro-osmotic scaling term, $D = 2en_o\phi_{max}D_h/\mu v_{eo}$
D_h	hydralic diameter (m)
K	non-dimensional Debye–Huckel parameter, $K = \kappa D_h$
L	characteristic length for Nusselt and Rayleigh numbers
Nu	Nusselt number, $Nu = hL/k_{air}$
P	non-dimensional pressure $P = pD_h/\mu v_{eo}$
Pe	Peclet number, $Pe = \rho c_p D_h v_{eo}/k$
P_{eo}	power required to generate electro-osmotic flow
Q	volume flow rate (μl/min)
Ra	Rayleigh number, $Ra = g\beta(T_{surf} - T_0)L^3/(k\mu/\rho^2 C_p)$
Re	Reynolds number, $Re = \rho v_{eo} D_h/\mu$
T	temperature (K)
V	non-dimensional velocity, $V = v/v_{eo}$
X, Y, Z	non-dimensional coordinate directions, $X = x/D_h, Y = y/D_h, Z = z/D_h$
c_p	specific heat (J/kg K)
e	electron charge, 1.6021×10^{-19} C
h	convective heat transfer coefficient (W/m^2 K)
k	thermal conductivity (W/m K)
k_B	Boltzmann constant, 1.3805×10^{-23} J/mol K
l_{xf}	channel half width (m)
l_{yf}	channel half height (m)
l_z	length of the channel in the z direction (m)
n_o	average ionic concentration ($1/m^3$)
p	pressure (Pa)
q	volumetric heat generation (W/m^3)
t	time (s)
v	velocity (m/s)
v_{eo}	electro-osmotic mobility, $v_{eo} = \varepsilon\varepsilon_0\zeta\phi_{max}/\mu l_z$
x, y, z	coordinate directions (m)

Greek symbols

Φ	non-dimensional applied electric field, $\Phi = \phi/\phi_{max}$
Ψ	non-dimensional electrostatic potential in the double layer, $\Psi = e\psi/k_B T$
Z	non-dimensional zeta potential, $\zeta = e\zeta/k_B T$
ε	dielectric constant of the medium
ε_0	permittivity of a vacuum, 8.854×10^{-12} C/V m
$\in$	emmisivity
ϕ	applied electric field (V)
ϕ_{max}	applied electro-osmotic driving voltage (V)
κ	Debye–Huckel parameter, $\kappa = (2n_o e^2/\varepsilon\varepsilon_0 k_B T)^{1/2}$
λ_t	total conductivity of the microchannel (1/Ωm)
N	radiative to conductive heat transfer ratio, $N = \sigma q^3 D_h^7 k_s^4$
μ	viscosity (kg/ms)
θ	non-dimensional temperature, $\theta = Tk_s/(qD_h^2)$
ρ	density (kg/m^3)
σ	Stefan–Boltzmann constant, 5.670×10^{-8} $W/(m^3\ K^4)$
τ	non-dimensional time $\tau = tv_{eo}/D_h$
ψ	electrostatic potential in the double layer (V)
ζ	zeta potential (V)

Subscripts

h	heater
f	fluid
o	atmospheric conditions
s	solid

Superscript

∼	non-dimensional parameter

due to the inherently high surface area to volume ratio, makes these microscale reactor devices extremely attractive.

Many studies have investigated methods of performing the controlled thermal cycling, like that required by the PCR, in microscale reactors. Simpler devices, such as that presented in [10], could perform PCR on a chip, however the thermal cycle was done externally by putting the chip in a commercial oven and taking it out periodically. Martin et al. [4] used 5 W heating cartridges and a series of cooling fins to actively control three different temperature zones, corresponding to the three stages of the PCR, on the same substrate. The reaction was then accomplished by forcing the reagents flowing through a single reaction channel that repeatedly passed in and out of the three zones. Daniel et al. [5] reported very high speed thermal cycling in silicon micro chambers using a heating element and an attached heat sink. They reported a steady state power load (i.e. power required to maintain the system at the desired temperature) between 1 and 2 W per chamber over the temperature range of interest. Recently Lao et al. [13] presented a device which uses integrated heaters to accomplish PCR like cycling of a 20 μl glycerol sample with steady state power loads between 1 and 2.5 W. Though the cycling is accomplished in different

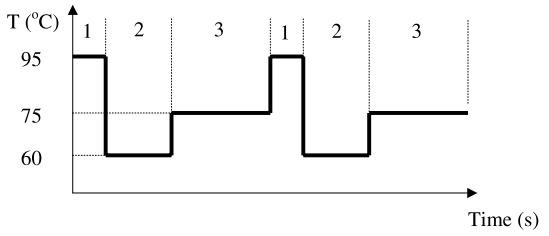

Fig. 1. Typical thermal cycle used for the polymerase chain reaction (two complete cycles shown).

ways, most studies have stated a preference for silicon-based substrates because of its high thermal conductivity ($\approx$148 W/m K) allows for uniform heating and rapid heat transfer.

Sample transport through these thermal cyclers also varies dramatically from study to study. In many devices an externally applied pressure difference is used via either a syringe [7], pump [4] or vacuum source [9]. Burns et al. [8] described a thermocapiliary pump which uses an applied temperature gradient to induce changes in the contact angle and surface tension between advancing and receding ends of discrete drops. The result is an internal pressure gradient that propels the drop forward. Their results suggest that a temperature difference on the order of 20–40 °C is required to provide motion. Electro-osmotic and electrophoritic flow [14–18], where an applied electric potential difference induces fluid motion, are becoming more and more common as a method of fluid transport in such devices. These electrokinetic methods offer significant advantages in that precise control over flow rates and species transport can be accomplished in complex geometries by simply manipulating applied voltages [15,17].

While micro-manufacturing techniques have allowed for the construction of the above devices to an extremely fine scale, a bottleneck which is likely to limit their evolution into fully stand alone, microscale biomedical or biochemical analysis systems are the high voltage and power requirements. The current–voltage and power requirements generally exceed what can be provided by a small (say, a 9 V) battery for extended periods of time. Consequently, all the aforementioned devices require external power sources for heating, cooling and for inducing flow.

The purpose of this study is to develop a three-dimensional numerical model of a proposed continuous flow microchannel thermal cycling reactor (US patent pending), with the goal of determining the optimum conditions that will maximize cycle speed and reaction output, while minimizing power and voltage requirements. The effects of the channel size, the construction material, the heater power and heater layout, and the applied voltage (for generating electro-osmotic flow) on the performance of the reactor will be investigated using a specially developed, in-house written, finite element code. The results will provide practical insight into how construction and operational changes are likely to affect reactor efficiency as well as provide fundamental information regarding the temperature profile within both the fluid and solid regions of the microchannel reactor and how effectively and accurately it can be controlled.

2. Numerical model

The study of heat transfer in microchannels began in earnest during the 1980s when direct liquid cooling emerged as a promising thermal management technique for electronic components [19]. Since that time numerous studies have been conducted on the heat transfer qualities of both liquid [20,21] and gas (for example [22]) flows through microchannels. Other recent studies [23,24] have examined, both experimentally and numerically, the transient response of microchannel heat sinks with the goal of determining the optimum conditions that promote electronic cooling using pressure driven flow. To date, however, very little work has been done on either numerical modeling of microchannel reactors or heat transfer in electro-osmotically driven flows.

Figs. 2(a) and (b) show cross-sectional views of the microchannel thermal cycling reactor to be modeled in this study. The device is constructed using a three-substrate approach where the channel and reservoir layout is etched into the middle substrate (shown in Fig. 2(a)) and the upper and lower substrates are bonded to the upper and lower surfaces of the middle substrate to form the enclosed channel (shown in Fig. 2(b)). In general the upper, middle and lower substrates could be the same or a different material. As is shown in Fig. 2(a), the reactor layout consists of parallel microchannels between the sample and product reservoirs. A series of embedded electric heaters are located along the length of each channel and are used to perform the thermal cycling. Fig. 2(b) shows a cross-section of a single channel and the location of the integrated electric heaters, bonded to the upper and lower substrates. Although only four individual channels are shown in Fig. 2(a), the actual reactor could consist of an array of parallel channels. Therefore, it was assumed that the majority of channels would be sufficiently isolated from the sides of the device so that the temperature distribution would be symmetrical about both the edge and vertical symmetry boundaries shown in Fig. 2(b).

2.1. Flow model

In general when a solid surface, such as the microchannel wall, meets an aqueous solution, a charge develops which is characterized by a surface electrostatic

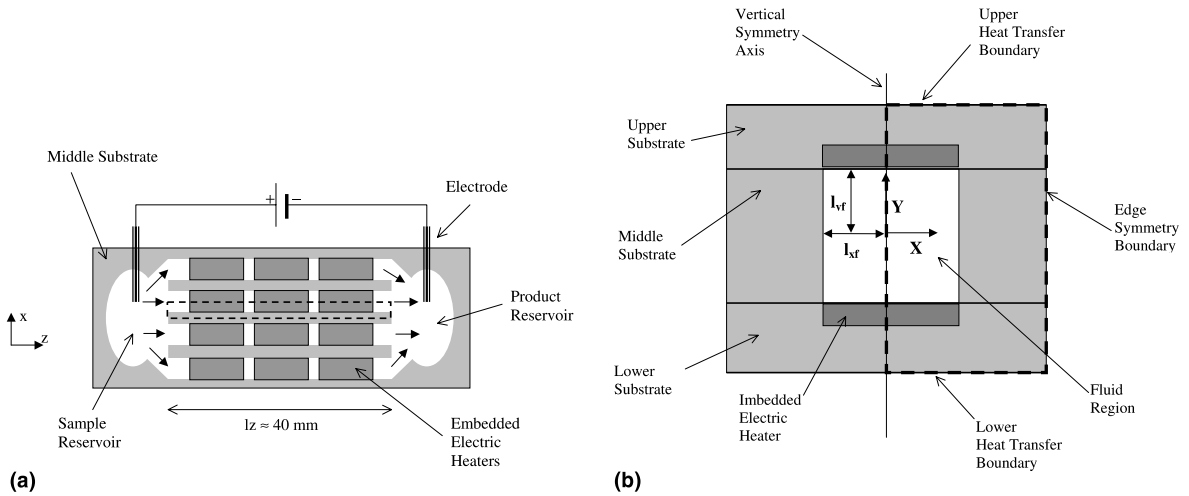

Fig. 2. Proposed microchannel thermal cycling reactor. Dashed line represents computational domain and filled arrowheads indicate flow direction. (a) Cut sectional top view showing middle substrate and embedded electric heater configuration along horizontal symmetry axis. (b) Cut section view of the x–y plane of a single channel at an arbitrary location along the z-axis.

potential called the ζ-potential. If the liquid contains a small number of ions, the electrostatic charges on the surface will attract counter ions in the liquid with a net force balanced by the thermal energy of the ions. The rearrangement of these ions in the liquid is known as the electrical double layer, or EDL. The potential field of EDL is described by Eq. (1),

$$\widetilde{\nabla}^2\Psi - K^2\sinh(\Psi) = 0, \tag{1}$$

where the upper case variables and the $\sim$ symbol represent the non-dimensional variables as outlined in the Nomenclature section. The details of the derivation of Eq. (1) are available elsewhere for the one-dimensional cases [25] and two-dimensional cases [26] and has been simply extended into the third dimension here as was done by Patankar and Hu [18]. As can be seen in the Nomenclature section, the double layer thickness, $1/\kappa$, is a function of temperature and thus in principle Eq. (1) should be reevaluated as the system temperature changes due to the thermal cycling. For the system considered here, where the ionic concentration is on the order of 1×10^{-3} mol/l (as will be discussed in Section 3.1) the double layer thickness varies from approximately 9.1 nm at 25 °C to 10.1 nm at 100 °C. This 1 nm change in the double layer thickness over the range of temperatures of interest would produce a negligible change in the velocity profile, and thus the use of an intermediate temperature, 75 °C, in evaluating the double layer thickness is justified. For further information on how the double layer influences the electro-osmotic velocity profile the reader is referred to the paper by Arulanandam and Li [14]. The proper boundary conditions for Eq. (1) are the non-dimensional ζ-potential, Z, at the liquid–solid interface ($\Psi = Z$ on $X = l_{xf}/D_h, Y = \pm l_{yf}/D_h$) and the appropriate symmetry condition along the vertical symmetry axis shown in Fig. 2(b) are $\partial\Psi/\partial X = 0$ on $X = 0$. Insulation type boundary conditions were applied at the channel inlet and exit ($\partial\Psi/\partial Z = 0$ on $Z = 0$, $Z = l_z/D_h$).

As mentioned earlier, electro-osmotic flow results from the application of an electrical body force to these free ions in the double layer region. In general the applied electric field can be described by Eq. (2),

$$\widetilde{\nabla}^2\Phi = 0. \tag{2}$$

At this point it is important to note at few assumptions that have been made in using Eq. (2) to describe Φ. The description of the applied electric field by the homogenous Poisson equation is a simplification valid only in cases where the bulk conductivity of the aqueous solution does not change significantly along the length of the channel. Secondly by decoupling the equations for the EDL and applied electric field, it has been assumed that the charge distribution near the wall is unaffected by the externally applied field. As is discussed by Saville [27] this assumption is generally valid so long as double layer thickness is not large, or equivalently the ionic concentration of the solution is not very low. As was discussed above the system considered here has a double layer thickness on the order of 10 nm, or approximately 1/5000 times the channel width, and thus this condition is met and the above decomposition is considered valid. To induce flow in the positive z direction a boundary conditions of $\Phi = 0$ and $\Phi = -1$ were applied at the inlet ($Z = 0$) and exit ($Z = l_z/D_h$) of the channel respectively. Insulation type boundary conditions were then

applied along the solid–liquid interface ($\partial\Phi/\partial X = 0$ on $X = l_{xf}/D_h$ and $\partial\Phi/\partial Y = 0$ on $Y = \pm l_{yf}/D_h$). As before a symmetry condition was applied along the symmetry axis ($\partial\Phi/\partial X = 0$ on $X = 0$).

Eqs. (3a) and (3b) represent the non-dimensional Navier–Stokes momentum equation, modified to account for the electrokinetic body force, and the continuity relation,

$$-\widetilde{\nabla}P + \widetilde{\nabla}^2 V + D\sinh(\Psi)\widetilde{\nabla}\Phi = 0, \tag{3a}$$

$$\widetilde{\nabla}\cdot V = 0. \tag{3b}$$

Generally, the electro-osmotic flow in microchannels is laminar flow with very low speed. Thus we consider only cases where $Re \ll 1$ and ignore the transient, convective and inertial terms in the Navier–Stokes equations, Eq. (3a). From Figs. 2(a) and (b), it is apparent that the flow is along the channel length direction, i.e., in the z direction, thus we ignore the x and y momentum equations. Finally in electro-osmotic flow both inlet and outlet reservoirs are typically maintained at atmospheric pressure and thus the pressure gradient term can be ignored (though for completeness it was included in the calculations done in this paper). As was shown by Herr et al. [16] this assumption is only valid in cases where surface properties of the channel wall are constant along the flow axis. Changes in the magnitude of the ζ-potential along this axis can lead to significant changes in the local magnitude of the electro-osmotic forcing term in Eq. (3a), inducing pressure gradients within the channel in order to satisfy continuity. To properly define the flow system, no slip boundary conditions were applied at the solid–liquid interface ($V_z = 0$ on $X = l_{xf}/D_h$, $Y = \pm l_{yf}/D_h$) and a symmetry condition was applied along the symmetry axis ($\partial V_z/\partial X = 0$ on $X = 0$). At both the channel inlet and outlet the condition $\partial V_z/\partial z = 0$ was applied.

Although the above equations were all solved in the 3D domain, it should be noted that in the case where the ζ potential is constant along the z-axis, the EDL Eq. (1) and flow Eqs. (3a) and (3b) essentially reduce to a 2D problem, i.e., the EDL field and the flow field remain constant along the z-axis. Similarly the applied electric field reduces to a 1D problem, remaining constant in the x–y plane.

2.2. Temperature model

As mentioned above the purpose of this model is to simulate the transient thermal behavior of the entire microchannel reactor and the temperature distribution must consider not only the fluid region but the surrounding solid substrate as well. As a result the convection–diffusion problem in the fluid region must be coupled with the purely diffusion problems in both the heaters and solid substrate. Within the fluid zone the non-dimensional energy equation takes the form shown below in Eq. (4a),

$$\left(\frac{k_f}{k_s}\right)Pe_f\left[\frac{\partial\theta}{\partial\tau} + V\cdot\widetilde{\nabla}\theta\right] = \left(\frac{k_f}{k_s}\right)\widetilde{\nabla}^2\theta. \tag{4a}$$

The solid zone itself can also be further subdivided into the substrate region, where the temperature distribution is governed by the simple transient diffusion Eq. (4b),

$$Pe_s\left[\frac{\partial\theta}{\partial\tau} + V\cdot\widetilde{\nabla}\theta\right] = \widetilde{\nabla}^2\theta \tag{4b}$$

and the heater zones which incorporates the uniform heat generation source term on the right-hand side,

$$\left(\frac{k_h}{k_s}\right)Pe_h\left[\frac{\partial\theta}{\partial\tau} + V\cdot\widetilde{\nabla}\theta\right] = \left(\frac{k_h}{k_s}\right)\widetilde{\nabla}^2\theta + 1. \tag{4c}$$

In all three zones the equations have been scaled by the thermal conductivity of the substrate region, k_s, for ease of computation.

Along the upper and lower surfaces of the computational domain, see Fig. 2(b), a boundary condition accounting for both convective heat transfer and radiation, described by Eq. (5), was used

$$\frac{\partial\theta}{\partial Y} + Bi(\theta - \theta_0) + \in N(\theta^4 - \theta_0^4) = 0. \tag{5}$$

To determine the convective heat transfer coefficient used in determining the Biot number in Eq. (5), two models were considered: the "upper and lower surfaces of a heated plate" relation from [28] and the "short vertical square cylinder" relation from [29], with the channel area divided by its perimeter as the characteristic dimension. In general the difference between these two models was not significant and thus the former, described by Eqs. (6a) and (6b) was chosen for the results presented here.

$$Nu_{upper} = 0.54Ra^{1/4}, \tag{6a}$$

$$Nu_{lower} = 0.27Ra^{1/4}. \tag{6b}$$

Using these relations, h was typically in the range of 6–15 W/m^2 K for both surfaces over the range of temperatures of interest, which is consistent with the values used by Jiang et al. [24]. As mentioned above symmetry conditions were placed along the edge symmetry boundary and vertical symmetry axis shown in Fig. 2(b).

In addition to the above, it was assumed that the channel inlet and outlet conditions matched the upstream and downstream reservoir temperatures, which were assumed to be sufficiently large and isolated from the reactor so that their temperatures would be maintained reasonably close to the atmospheric temperature. $\theta(\tau = 0) = \theta_0$ was applied as an initial condition indicating that the system was initially at the atmospheric temperature.

As is well known, viscosity, thermal conductivity and specific heat are all temperature dependent. Thus the full set of Eqs. (3a), (3b) and (4a)–(4c) would have to be solved at each time step to fully capture the effects of the changing temperature on the thermophysical properties. Such a scheme was found to be computationally too expensive and thus all thermal properties were evaluated at an intermediate temperature. Since we are mainly concerned with the average behavior over the course of a thermal cycle, this assumption was not deemed too significant. Another, more fundamental, assumption implied by the above model, specifically Eqs. (3a), (3b) and (4a), is incompressibility. The rapid thermal cycling in the relatively enclosed microchannel does introduce the possibility that the volumetric expansion of the liquid may be significant, however there are two important considerations that allow us to ignore this effect. Firstly the thermal cycles to be carried out in the reactor (for example Fig. 1) are cyclical in nature and any expansion of the fluid during a heating period is necessarily countered with an equivalent contraction during a cooling period, resulting in no net flow. Secondly the magnitude of the expansion during the cycle is very small, less than $\pm 1\%$ about the mean volume, and an order of magnitude analysis has shown that the average velocity of the expansion is typically less than 2% of the electro-osmotic velocity.

2.3. Numerical algorithm

The flow and temperature models were solved with an in-house written code using the finite element method [30] by discretizing the computational domain using 27-noded triquadratic elements. The flow domain was discretized first and solutions for Ψ, Φ and V were obtained. The fact that the most significant gradients in both Ψ and V occur within or near the double layer region, can lead to computational difficulties due to the excessive amount of grid refinement which may be needed. Previous studies have resolved this problem by either assuming a relatively thick double layer [18], or equivalently a very low concentration solution, or by ignoring the double layer region and applying the electro-osmotic slip condition at the wall [15,17]. In this study the problem was combated by introducing an independent level of grid refinement within a band of thickness 3/K from the solid–liquid interface. This method of grid refinement in the x–y plane ensures that solution accuracy does not suffer when thin double layers, or higher and more realistically concentrated solutions, are encountered. Once a solution to the flow field was obtained, the original computational grid was extended to encompass the temperature field. Further grid refinement along the z-axis was used in the regions near the beginning and end of the heater zones, where temperature gradients were found the strongest.

The thermal cycling in the reactor was simulated by independently controlling each heater using an on/off algorithm. At each time step the average temperature of each heater was monitored to see if it had reached the desired temperature plateau. If the average temperature of the heater was below this goal temperature, the source term, shown in Eq. (4c), was included (indicating an on phase) and if it was above the source term was omitted (indicating an off phase). Once all the heaters had reached the desired temperature the system was maintained at that level for the desired dwell time using the same on/off algorithm as above. The temporal derivatives in Eqs. (4a)–(4c) were discretized using an implicit Euler method and the system was solved at each time step using a biconjugate gradient solver.

3. Numerical simulation

As mentioned earlier, the purpose of study was to develop a 3D numerical model of the proposed microchannel thermal cycling reactor, shown in Figs. 2(a) and (b), with the goal of determining the optimum conditions for promoting rapid thermal cycling, while minimizing the total power and voltage requirements. For the purpose of this simulation it was assumed that the heaters were made of platinum with the following thermal properties: $\rho_h = 21\,450$ kg/m^3, $C_{p_h} = 133$ J/kg K and $k_h = 71.6$ W/m K. The fluid was assumed to be an aqueous solution of with an ionic concentration of 10^{-3} M, which is on the order of typical buffer solutions used in the applications of interest. All thermophysical properties were taken from Incroperta and Dewitt [28] and, as mentioned in Section 2.2, were evaluated at an intermediate temperature and held constant throughout the simulations. All simulations presented here were conducted with a constant cover plate thickness (i.e. the distance from the top/bottom of the fluid channel to the upper/lower convective boundary) of 200 μm and a 100 μm distance between parallel channels.

3.1. Flow simulations

In Fig. 3 the relationship between applied electro-osmotic driving voltage, ϕ_{max}, and volume flow rate, Q, is shown for channels of different size. The ζ-potential at the liquid–glass interface was fixed at -56 mV, consistent with the value reported in [31]. The flow simulations yielded a plug flow type velocity profile similar to that described by Arulanandam and Li [14]. This velocity profile can have significant advantages in terms of transport in that all species are convected with the same velocity, independent of their location in the channel cross-section.

Of the most interest in Fig. 3 is the scale of the volume flow rates obtained at the given voltages, which

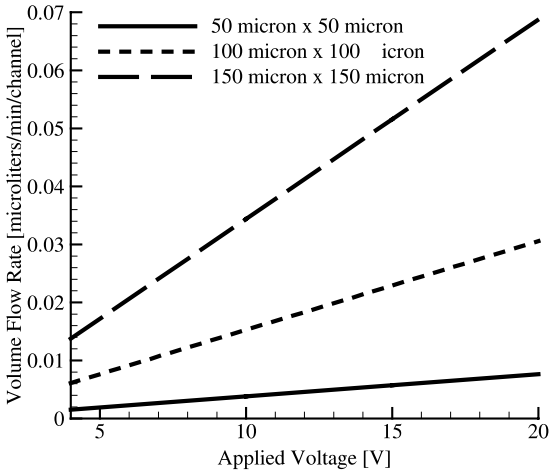

Fig. 3. Influence of total applied electroosmotic driving voltage on per channel volume flow rate. Results shown are for a fluid of concentration 10^{-3} M in a 40 mm long glass channel ($\zeta = -56$ mV).

vary from approximately 2–70 nl/min per channel. The total voltages, rather than the lengthwise gradient, are given on the independent axis to emphasize the fact that the applied potential can be produced by low cost sources such as batteries. However, it should be pointed out that these specific results are obtained for the 40 mm long channels used in the study. To extrapolate these results to different channel lengths the applied voltage gradient should be used.

Also of interest in Fig. 3 is the linear increase in the volume flow rate with increasing $\phi_{\max}$, and the significant increase in volume flow rate with channel cross-sectional area. The latter of these does not come without a price however in that increasing the channel cross-sectional area necessarily decreases the electrical resistance leading to an increase in the require electro-osmotic pumping power, as described by Eq. (7) for this application,

$$P_{\mathrm{eo}} = \frac{\phi_{\max}^2 \lambda_{\mathrm{t}} A_{\mathrm{c}}}{l_z}. \tag{7}$$

P_{eo} however is significantly lower than the power required in performing the thermal cycling and therefore is not considered a serious limitation.

3.2. Thermal simulations

Figs. 4(a) and 5(a) show the temperature contours in the microchannel reactor at a cross-section in the x–y plane located at the midpoint between the channel entrance and exit, and along the channel length at the horizontal symmetry plane, during a heating stage. Figs. 4(b) and 5(b) show similar contours during a cooling stage. The substrate material for this simulation

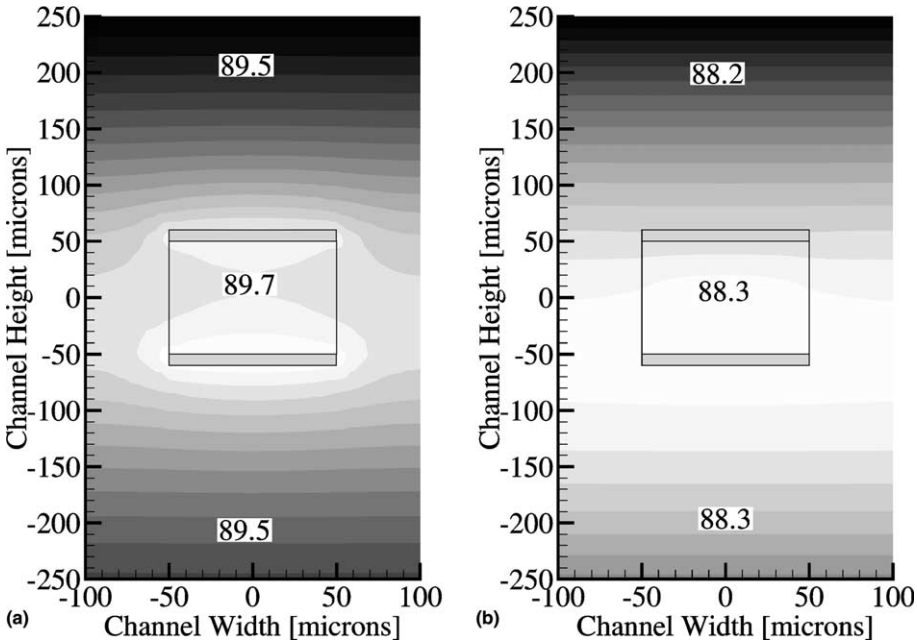

Fig. 4. Temperature contours in the x–y plane at $z \approx 20$ mm for a 30 mW/channel peak load, glass microchannel reactor during: (a) a heating phase and (b) a cooling phase. Lighter colors represent warmer temperatures and contour labels show temperature in degree Celsius.

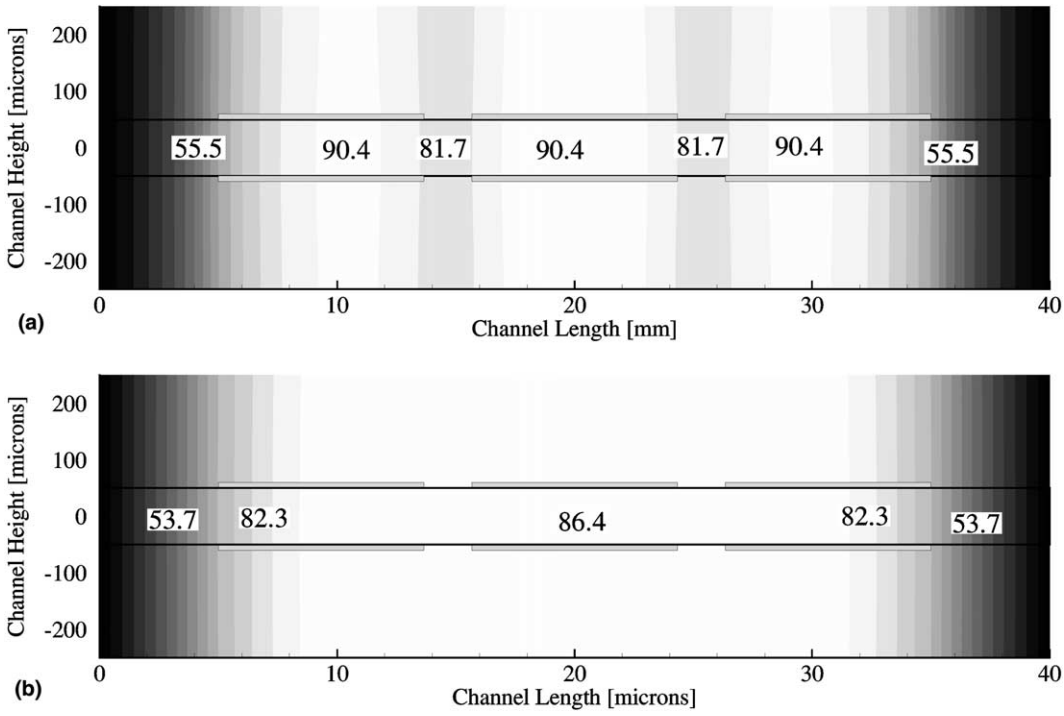

Fig. 5. Temperature contours along the z-axis showning along the vertical symmetry axis for a 30 mW/channel peak load, glass microchannel reactor during: (a) a heating phase and (b) a cooling phase. Lighter colors represent warmer temperatures and contour labels show temperature in degree Celsius.

is glass ($\rho_s = 2225$ kg/m^3, $C_{p_s} = 835$ J/kg K, $k_s = 1.4$ W/m K), the channel size is 100 μm × 100 μm and the peak power supply was 30 mW/channel. The gray boxes indicate the heater regions, while the thick dark lines show the solid–liquid boundary. Darker regions represent colder temperatures and contour labels indicate temperature in degree Celsius.

By comparing both Figs. 4(a) and (b) with Figs. 5(a) and (b), it is apparent that the more significant temperature gradients occur along the z (lengthwise) axis, whereas temperature is relatively uniform within the x–y cross-section. This is a result of the extremely high length to width ratio of the channel yielding a much smaller diffusion length scale in the x–y plane than along the z-axis.

4. Optimized microchannel thermal cycling reactor

As mentioned in Section 1, a potential bottleneck limiting the development fully portable, low cost microdevices are the relatively large power requirements of the reactors. Of those devices reported in the literature, the majority have steady state power loads on the order of 1 or 2 W or greater, for example [4,5,13], which is difficult to maintain for long periods of time using off-the-shelf batteries. As such the main thrust of this research was to use the numerical code described in Section 2 to determine the optimum conditions permitting low power thermal cycling in a microchannel reactor.

4.1. Influence of peak heating power on cycle time

For a passively cooled system, like the proposed reactor, an electrical power load only exists during the heating and holding stages of a thermal cycle like that shown in Fig. 1. Here the peak heater power is defined as that used during a heating phase and the steady state power load as that required to maintain the system at the desired dwell temperature. While the peak heater power influences the rate at which heating can be accomplished, the steady state power load is a function of the system geometry, substrate thermal properties and the convective/radiative heat transfer from the surfaces.

Fig. 6 compares the average temperature at the centerline of the channel over the heated section of the channel for simulations conducted at peak heater powers of 20, 30 and 40 mW/channel for a 50×50 μm^2 channel in a glass substrate with the same material properties as those mentioned in Section 3.2. Note that for completeness the results presented in Fig. 6 include

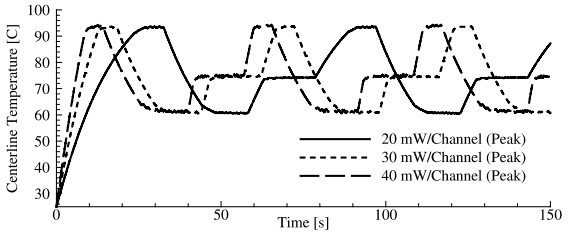

Fig. 6. Simulation of the PCR cycle showing influence of peak heater power on cycle time. Shown is the average centerline temperature in a 50×50 μm^2 channel and a 4 V total electro-osmotic driving force.

the initial temperature ramping stage (from T_0) as well as repeated cycle calculations. For this geometry the steady state power loads (as recorded during the three dwell stages) were 17 mW/channel at 95 °C, 11 mW/channel at 75 °C and 7 mW/channel at 60 °C. Since 20 mW/channel is close to the steady state power load of 12 mW/channel (i.e. the minimum power requirement of the heater to reach the required 95 °C), a significant decrease in the cycle time is observed when the peak power load is increased to 30 mW/channel. As the peak heater power is further increased, to 40 mW/channel, the cycle time is again decreased however the improvement is less significant.

Fig. 7 further highlights this trend by showing the decrease in the total cycle time, including dwell times as outlined in Section 1, with increasing peak heater power for a number of different channel sizes but the same inter-channel spacing and upper/lower substrate thickness. In calculating the cycle times for Fig. 7, the initial cycle where the system is ramped up from T_0, has been ignored and thus the results represent the quasi-steady cycle time. As can be seen increasing the peak heater power is only effective to a point, above which further increases do not significantly reduce the cycle time because the total cycle time is now dominated by the required cooling time. It is crucial to consider both this maximum effective value and the minimum heater power requirement to reach the highest temperature specified in the cycle, as these values provide a range of heater powers over which the reactor will operate most effectively with the low heating power.

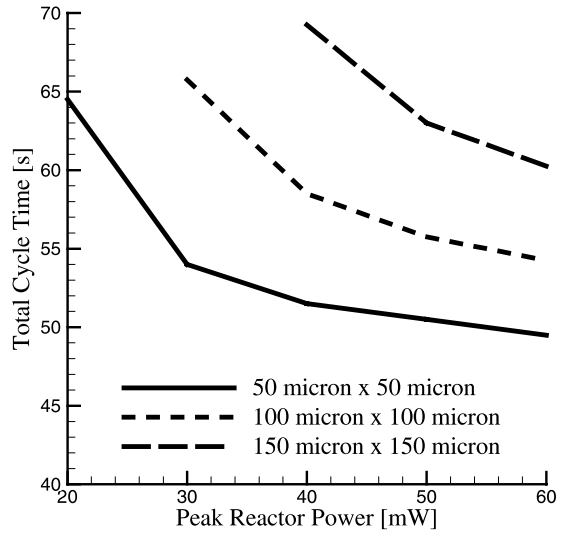

Fig. 7. Influence of peak reactor power on cycle time. Electro-osmotic driving voltage for this case is 4 V.

4.2. Influence of channel size on cycle time

Fig. 7 also serves to demonstrate the relationship between the channel cross-sectional dimensions and the cycle time. As channel size is increased the thermal capacitance of the system is also increased resulting in longer heating and cooling times and therefore slower thermal cycling. The increased heat loss for larger channels, due to the larger area in contact with the atmospheric reservoirs and the larger upper/lower heat transfer surfaces, tend to make this difference more significant at lower peak heater powers. While decreasing the channel size does decrease the cycle time it is important to note that, referring back to Fig. 3, this necessarily results in a decrease in the volume flow rate proportional to the cross-sectional area. The steady state power loads for the 100 μm × 100 μm channel was 23, 14 and 10 mW/channel at the 95, 75 and 60 °C holding plateaus. At the same holding plateaus the 150 μm × 150 μm channel had steady state power loads of 31, 19 and 12 mW/channel.

4.3. Influence of substrate thermal properties on cycle time

Fig. 8 compares the average centerline temperature, over the heated section of the channel, for a 50 μm × 50 μm channel at 20 mW/channel peak power for both a

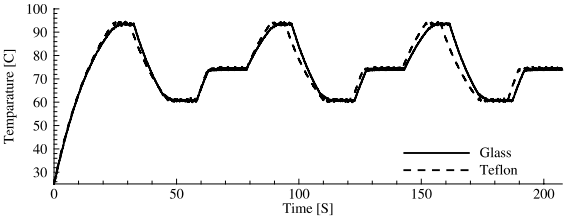

Fig. 8. Simulation of PCR cycle comparing a glass substrate with a low thermal conductivity polymeric substrate (Teflon is used as an example here). Shown is the average centerline temperature in a 50×50 μm^2 channel and a 4 V total electro-osmotic driving force.

glass substrate and a low thermal conductivity polymeric substrate (Teflon, $\rho_s = 2170$ kg/m^3, $C_{ps} = 1004$ J/kg K, $k_s = 0.25$ W/m K [32], is used as an example here). Both materials are similar in terms of density and specific heat, however k_s for Teflon is approximately 1/5th that of glass. As can be seen the lower thermal conductivity material tends to exhibit a slightly faster cycle time. This can be attributed to reduced conduction along the z-axis (Fig. 2(a)) and therefore better thermal isolation of the effective reaction zone from the atmospheric reservoirs. Note that while this tends to promote faster heating it adversely affects the cooling time and as such much of the gains made during the heating phase are lost during cooling stages. Simulations conducted for higher thermal conductivity substrates, like silicon, revealed the increased axial conduction and therefore increased heat loss to the atmospheric reservoirs resulted in significantly higher heater power requirements, making lower thermal conductivity substrates preferable for low power thermal cycling.

4.4. Importance of heater configuration

In order to create the largest possible effective reaction zone, a uniform temperature profile is desired along as much of the microchannel as possible. Fig. 9(a) and (b) compare the temperature profile at the three dwell temperatures detailed in Fig. 1, for the 3×2 heater configuration (a) shown in Fig. 2(a) with an equivalent 1×2 heater configuration where a single heater (b) on both the top and bottom is used. While the gaps between the heaters in the 3×2 produce some regions of lower temperature, most prominently at the 95 °C plateau, the temperature varies only 4 °C over the inner 25 mm of the channel at the 95 °C plateau and ±2 °C at 60 °C plateau.

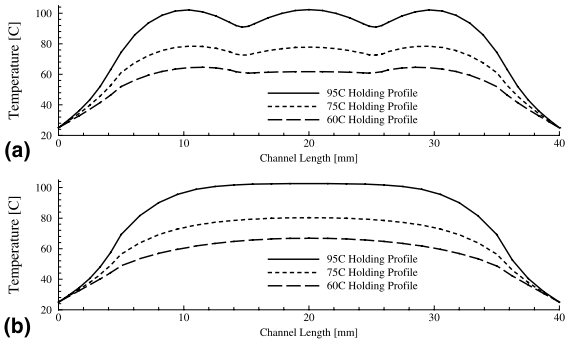

Fig. 9. Comparison of centerline temperature profiles along the length of the channel during the three holding phases of the PCR reaction: (a) 3×2 heater configuration, (b) 1×2 heater configuration. Results shown are for a 150×150 μm^2 channel and a 4 V total electro-osmotic driving force.

The single heater does not have the "cold spots" however produces a significantly more curved profile with variations of approximately ±8 and ±5 °C at the same plateaus. The result of the lower temperatures near the edges of the actively heated region is that the effective reaction zone for a single heater configuration is significantly smaller, thus less of the sample is exposed to the optimum temperatures and the total yield of the reactor is reduced.

4.5. Brief comments on the power consumption of a multichannel device

The results presented above consider the per channel power consumption of the optimized device. To consider the total power consumption of a multichannel device we consider the number of channels required to hold a sample size comparable to the other micro-reactors mentioned earlier. The 150 μm × 150 μm channel device has an effective sample volume (volume within the effective reaction zone as discussed in Section 4.4) of 0.56 μl per channel and a steady state power load of 31 mW/channel at 95 °C as mentioned in Section 4.2. Thus to handle a volume comparable to the 1.5 μl sample used in [5] would require a 3-channel device for a total steady state power load of 93 mW in contrast to the approximate 2 W reported in that work [5]. Similarly the 20 μl sample size considered in [13] would require approximately 36 channels and a steady state power load of 1.1 W instead of the 2.4 W reported there.

5. Conclusions

Advancements in the manufacturing of microfluidic components are leading towards the development of fully integrated and stand-alone microscale biomedical analysis systems. In order to develop portable microscale reactors that can be operated for extended periods using low cost batteries advanced thermal modeling and management techniques must be developed. This study was initiated to determine the minimum heating power requirements of a proposed thermal cycling microchannel reactor by developing a numerical model.

Based on the numerical model a general thermal cycling microchannel reactor design was developed which allows for relatively rapid thermal cycling at peak heater powers as low as 20 mW/channel, with even lower power loads during the holding stages. It was found that a narrow range of optimal reactor heating power exists, below which the reactor will not be able to reach and maintain at the highest temperature plateaus, and above which additional supplied power no longer provides significant benefit in terms of reducing the total cycling time. It was found that this optimal power range was

largely influenced by several factors, however most importantly by the channel construction material, as materials with higher thermal conductivity necessarily led to significantly higher power requirements. Heater configuration was found to influence the size of the effective reaction zone, for example, the 3×2 heater configuration generated a larger uniform temperature zone when compared to the 1×2 configuration. Finally, the results of flow simulations revealed that an electro-osmotically driven flow could yield an output of this type of reactor on the order of 2–70 nl/min per channel.

Acknowledgements

The authors wish to thank the financial support of the Natural Sciences and Engineering Research Fund through a scholarship to David Erickson and through a research grant to D. Li.

References

[1] S.C. Jacobson, J.M. Ramsey, Integrated microdevice for DNA restriction fragment analysis, Anal. Chem. 68 (5) (1996) 720–723.
[2] L.J. Kricka, X. Ji, O. Nozaki, S. Heyner, W.T. Garside, P. Wilding, Sperm testing with microfabricated glass-capped silicon microchannels, Clin. Chem. 40 (9) (1994) 1823–1824.
[3] L.J. Kricka, I. Faro, S. Heyner, W.T. Garside, G. Fitzpatrick, P. Wilding, micromachined glass-glass microchips for in vitro fertilization, Clin. Chem. 41 (9) (1995) 1358–1359.
[4] M.U. Martin, A.J. de Mello, A. Manz, Chemical amplification: continuous flow PCR on a chip, Science 280 (1998) 1146–1148.
[5] J.H. Daniel, S. Iqbal, R.B. Millington, D.F. Moore, C.R. Lowe, D.L. Leslie, M.A. Lee, M.J. Pearce, Silicon microchambers for DNA amplification, Sensors Actuators A 71 (1998) 81–88.
[6] J. Cheng, M.A. Shoffner, K.R. Mitchelson, L.J. Kricka, P. Wilding, Analysis of ligase chain reaction products amplified in a silicon-glass chip using capillary electrophoresis, J. Chromatogr. A 732 (1996) 151–158.
[7] P. Wilding, L.J. Kricka, J. Cheng, G. Hvichia, M.A. Scoffner, P. Fortina, Integrated cell isolation and polymerase chain reaction analysis using silicon microfilter chambers, Anal. Biochem. 257 (1998) 95–100.
[8] M.A Burns, C.H. Mastrangelo, T.S. Sammarco, F.P. Man, J.R. Webster, B.N. Johnson, B. Foerster, D. Jones, Y. Fields, A.R. Kaiser, D.T. Burke, Microfabricated structures for integrated DNA analysis, Proc. Natl. Acad. Sci. USA 93 (1996) 5556–5561.
[9] E.T. Lagally, P.C. Simpson, R.A. Mathies, Monolithic integrated microfluidic DNA amplification and capillary electrophoresis analysis system, Sensors Actuators B 63 (2000) 138–146.
[10] L.C. Waters, S.C. Jacobson, N. Kroutchinina, J. Khandurina, R.S. Foote, J.M. Ramsey, Multiple sample PCR amplification and electrophoritic analysis on a microchip, Anal. Chem. 70 (24) (1998) 5172–5176.
[11] M.A. Northrup, B. Benett, D. Hadley, P. Landre, S. Lehew, J. Richards, P. Stratton, A miniature analytical instrument for nucleic acids based on micromachined silicon reaction chambers, Anal. Chem. 70 (5) (1998) 918–922.
[12] A.T. Woolley, D. Hadley, P. Landre, A.J. de Mello, R.A. Mathies, M.A. Northrup, Functional integration of PCR amplification and capillary electrophoresis in a microfabricated DNA analysis device, Anal. Chem. 68 (23) (1996) 4081–4086.
[13] A.I.K. Lao, T.M.H. Lee, I.-M. Hsing, N.Y. Ip, Precise temperature control of microfluidic chamber for gas and liquid phase reactions, Sensors Actuators 84 (2000) 11–17.
[14] S. Arulanandam, D. Li, Liquid transport in rectangular microchannels by electroosmotic pumping, Colloid. Surf. A 161 (2000) 89–102.
[15] S.V. Ermakov, S.C. Jacobson, J.M. Ramsey, Computer simulations of electrokinetic injection techniques in microfluidic devices, Anal. Chem. 72 (15) (2000) 3512–3517.
[16] A.E. Herr, J.I. Molho, J.G. Santiago, M.G. Mungal, T.W. Kelly, M.G. Garguilo, Electroosmotic capillary flow with nonuniform zeta potential, Anal. Chem. 72 (5) (2000) 1053–1057.
[17] S.V. Ermakov, S.C. Jacobson, J.M. Ramsey, Computer simulations of electrokinetic transport in microfabricated channel structures, Anal. Chem. 70 (21) (1998) 4494–4504.
[18] N.A. Patankar, H.H. Hu, Numerical simulation of electroosmotic flow, Anal. Chem. 70 (9) (1998) 1870–1881.
[19] D.B. Tuckerman, R.F.W. Pease, High-performance heat sinking for VLSI, IEEE Electro Device Lett. EDL-2 (1981) 126–129.
[20] Gh.M. Mala, D. Li, D. Dale, Heat transfer and fluid flow in microchannels, Int. J. Heat Mass Transfer 40 (13) (1997) 3079–3088.
[21] W. Qu, Gh.M. Mala, D. Li, Heat transfer for water flow in trapezoidal silicon microchannels, Int. J. Heat Mass Transfer 43 (2000) 3925–3936.
[22] G. Tunc, Y. Bayazitoglu, Heat transfer in microtubes with viscous dissipation, Int. J. Heat Mass Transfer 44 (2001) 2395–2403.
[23] J.R. Rujano, M.M. Rahman, Transient response of microchannel heat sinks in a silicon wafer, J. Electronic Packaging 119 (1997) 239.
[24] L. Jiang, M. Wong, Y. Zohar, Transient temperature performance of an integrated micro-thermal system, J. Micromech. Microeng. 10 (2000) 466–476.
[25] R.J. Hunter, Zeta Potential in Colloid Science, Academic Press, London, 1981.
[26] Gh.M. Mala, C. Yang, D. Li, Electrical double layer potential distribution in a rectangular microchannel, Colloid. Surf. A 135 (1998) 109–116.
[27] D.A. Saville, Electrokinetic effects with small particles, Annu. Rev. Fluid Mech. 9 (1977) 321–337.
[28] F.P. Incropera, D.P. DeWitt, in: Introduction to Heat Transfer, third ed., Wiley, New York, 1996, pp. 743–770.

[29] G.D Raithby, K.G.T. Hollands, Natural Convection, in: W.M. Rohsenow, J.P. Hartnett, Y.I. Cho (Eds.), Handbook of Heat Transfer, McGraw-Hill, New York, 1998, p. 4.28.
[30] J.C. Heinrich, D.W. Pepper, Intermediate Finite Element Method, Taylor & Francis, Philadelphia, 1999.
[31] D. Erickson, D. Li, C. Werner, An improved method of determining the ζ-potential and surface conductance, J. Colloid Interface Sci. 232 (1998) 186–197.
[32] A.L. Edwards, A compilation of thermal property data for computer heat-conduction calculations, UCRL-50589, 1969.